

# Effects of Thermal Annealing Upon the Morphology of Polymer–Fullerene Blends

By Eric Verploegen, Rajib Mondal, Christopher J. Bettinger, Seihout Sok, Michael F. Toney, and Zhenan Bao\*

Grazing incidence X-ray scattering (GIXS) is used to characterize the morphology of poly(3-hexylthiophene) (P3HT)–phenyl-C<sub>61</sub>-butyric acid methyl ester (PCBM) thin film bulk heterojunction (BHJ) blends as a function of thermal annealing temperature, from room temperature to 220 °C. A custom-built heating chamber for in situ GIXS studies allows for the morphological characterization of thin films at elevated temperatures. Films annealed with a thermal gradient allow for the rapid investigation of the morphology over a range of temperatures that corroborate the results of the in situ experiments. Using these techniques the following are observed: the melting points of each component; an increase in the P3HT coherence length with annealing below the P3HT melting temperature; the formation of well-oriented P3HT crystallites with the (100) plane parallel to the substrate, when cooled from the melt; and the cold crystallization of PCBM associated with the PCBM glass transition temperature. The incorporation of these materials into BHJ blends affects the nature of these transitions as a function of blend ratio. These results provide a deeper understanding of the physics of how thermal annealing affects the morphology of polymer–fullerene BHJ blends and provides tools to manipulate the blend morphology in order to develop high-performance organic solar cell devices.

## 1. Introduction

Solution-processable organic photovoltaics (OPVs) show great promise for providing a cost-effective route for creating lightweight and flexible solar energy conversion devices.<sup>[1–3]</sup> Polymer–fullerene bulk heterojunctions (BHJ) have been intensely studied over the past decade for use as the active layer in such devices; one of the most popular blends consists of poly(3-hexylthiophene) (P3HT), as the electron-donor phase, and phenyl-C<sub>61</sub>-butyric acid methyl ester (PCBM), as the electron-acceptor phase. The optimization of bulk heterojunction blend

morphologies is critical in order to achieve high performance in OPV devices.<sup>[4]</sup> The morphology and molecular packing of both the acceptor and donor within their respective domains must be optimized for maximum charge-carrier mobilities and exciton transport (diffusion). In addition, the nanophase segregated heterojunction domain size must be less than the exciton diffusion length in order for efficient conversion of adsorbed photons into electrical current.

Thermal,<sup>[5–8]</sup> electric field,<sup>[9]</sup> and solvent<sup>[10,11]</sup> annealing have shown utility for manipulating and improving BHJ morphologies and performance. Additionally, careful choice of the solvent used to deposit the polymer–fullerene thin films is of critical importance for controlling the morphology.<sup>[12–14]</sup> Typically, extended thermal annealing or excessively slow solvent evaporation lead to unfavorable coarsening of the acceptor and donor domains, resulting in phase segregation at length scales larger than the exciton diffusion length and consequently poor performance. Thus, it is

desirable to optimize the morphology/packing, e.g., increase the crystallinity of these domains – without allowing the size of the domains to grow larger than the exciton diffusion length. It is important to also consider the crystallographic orientation of the polymer component for effective charge transport to the electrodes. In semi-crystalline polythiophenes, high charge mobility occurs along the polymer chain backbone and parallel to the  $\pi$ – $\pi$  stacking direction of the thiophene rings. In BHJ solar cells the charge must travel perpendicular to the substrate in order to reach the electrodes, and therefore it is desirable for the  $\pi$ – $\pi$  stacking to be largely perpendicular to the substrate to allow for high mobility pathways to the electrodes (the chain backbones do not align in this orientation). In contrast, for organic field-effect transistor (OFET) applications, charge transport between the source and the drain occurs parallel to the substrate; thus, it is ideal for the backbones and the  $\pi$ – $\pi$  stacking directions to be parallel to the substrate.<sup>[15]</sup>

It is important to consider how the processing conditions affect the crystallization behavior of the blend components and impacts on the nanophase segregated domain size induced by the crystallization and the charge-carrier mobility within each domain. Currently, the knowledge as to how this component

[\*] Dr. E. Verploegen, Dr. R. Mondal, Dr. C. J. Bettinger, S. Sok, Prof. Z. Bao  
Department of Chemical Engineering  
Stanford University  
Stanford, CA 94305, USA  
E-mail: zbao@stanford.edu  
Dr. E. Verploegen, Dr. M. F. Toney  
Stanford Synchrotron Radiation Lightsource  
Menlo Park, CA 94025, USA

DOI: 10.1002/adfm.201000975

morphology is affected by the thermal annealing process is incomplete. Gaining a deeper understanding of these effects will allow for more efficient optimization of the processing conditions required to achieve the maximum performance from such devices. Differential scanning calorimetry (DSC) is commonly used in order to evaluate the thermal properties of the components used in BHJ solar cells, clearly revealing the melting points ( $T_m$ ) of the components and other first order phase transitions.<sup>[16–18]</sup> Often significant morphological rearrangements can occur when the annealing temperature is raised above certain second order transition temperatures, e.g., glass transition temperatures; therefore identifying these transitions is critical for understanding the effects of thermal processing upon the morphologies of these systems. Unfortunately, second order transitions are often difficult to resolve with DSC due to their low associated enthalpy. Additionally, DSC measures the thermal properties of the bulk material, but the phase behavior may be significantly different for thin films of the same material.

Grazing incidence X-ray scattering (GIXS) has been shown to be a useful tool for investigating the morphology of thin film polymer–fullerene BHJ blends.<sup>[10,19–21]</sup> Here we present a systematic study investigating the morphology of the bulk heterojunction blends and their individual components with GIXS both during the thermal annealing process (in situ heating) and after thermal annealing (films annealed with a thermal gradient) over a range of temperatures. To achieve the former we developed a heating chamber enabling in situ GIXS. This technique allows us to observe the molecular rearrangements during thermal annealing for both the P3HT and PCBM components, providing critical insights into the dynamics of the morphological evolution. We demonstrate how GIXS can be used to rapidly and systematically characterize the morphological evolution of polymer – fullerene BHJ blends during thermal annealing.

## 2. Results and Discussion

GIXS images of P3HT, 3:1 P3HT–PCBM blend, 1:1 P3HT–PCBM blend, 1:3 P3HT–PCBM blend, and PCBM thin films, as-cast and after thermal annealing at 220 °C are shown in Figure 1. For each thin film composition significant morphological rearrangements are observed after thermal annealing. Below, we will discuss the nature and significance of the observed changes. However, first, it is important to characterize the behavior of the individual components in order to understand the morphological behavior of the polymer–fullerene blends.

### 2.1. Thermal Annealing of P3HT Thin Films

Solutions of P3HT in chloroform were spin cast onto a bare silicon wafer, resulting in films with thicknesses of 20 to 25 nm. A GIXS image of an as-cast thin film is shown in Figure 1a. In this image a distinct peak (100) is observed at  $q = 0.38 \text{ \AA}^{-1}$ , along with several higher order reflections, indicating the presence of P3HT lamellae with spacing of  $16.7 \text{ \AA}$ . These

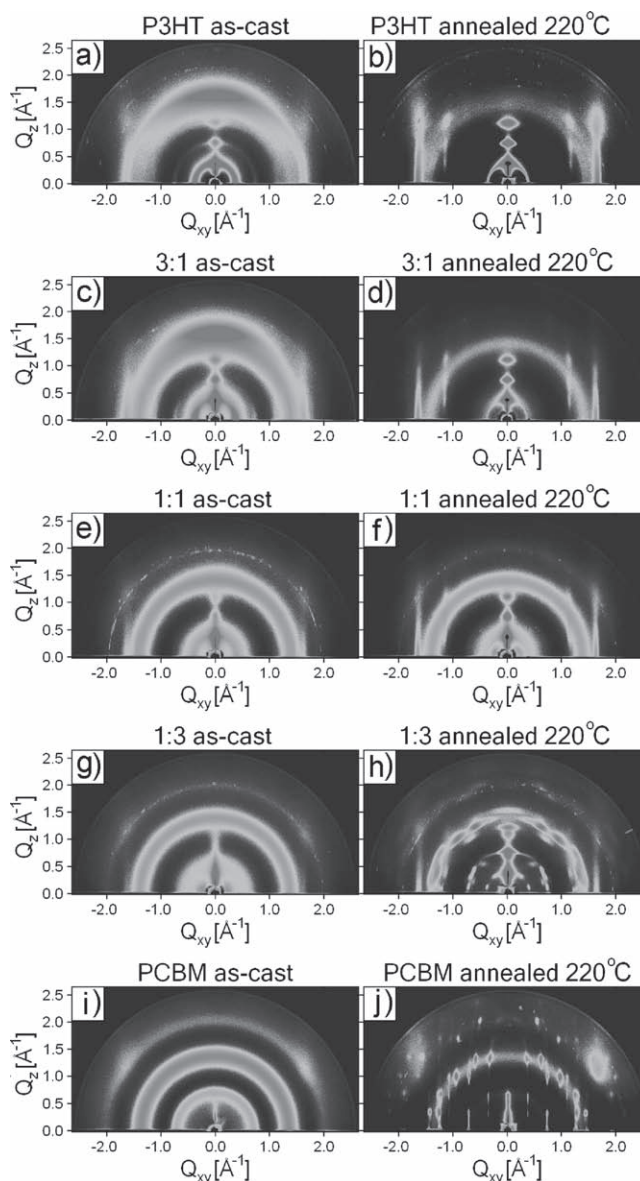
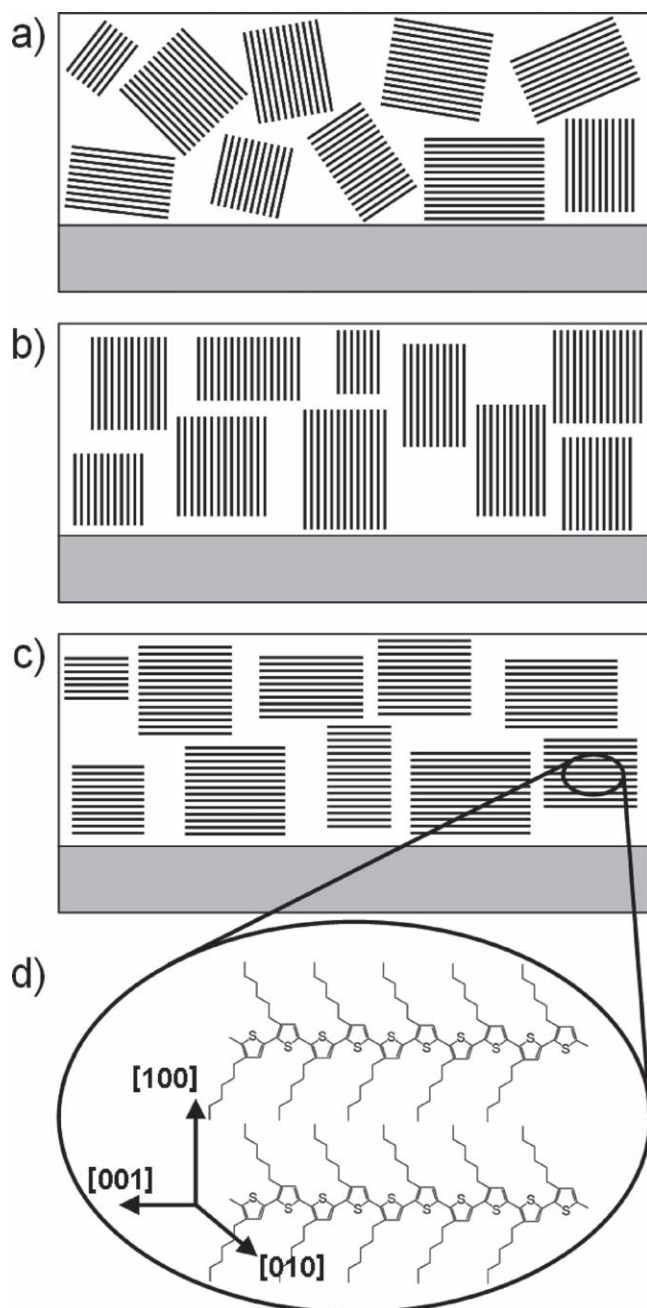


**Figure 1.** 2-D GIXS images of a) as-cast P3HT, b) P3HT annealed at 220 °C, c) as-cast 3:1 P3HT–PCBM blend, d) 3:1 P3HT–PCBM blend annealed at 220 °C, e) as-cast 1:1 P3HT–PCBM blend, f) 1:1 P3HT–PCBM blend annealed at 220 °C, g) as-cast 1:3 P3HT – PCBM blend, h) 1:3 P3HT–PCBM blend annealed at 220 °C, i) as-cast PCBM, and j) PCBM annealed at 220 °C.

peaks appear out-of-plane, approximately perpendicular to the substrate, indicating that the P3HT lamellae are predominantly oriented parallel to the substrate. The (200) peak at  $q = 0.75 \text{ \AA}^{-1}$ , was used for analysis due to the overlap of the specular reflectance with the (100) peak. The region selected for subsequent quantitative analysis is shown in Figure S1 of the supplementary information.

For the in situ heating experiments the films were heated at a rate of  $10 \text{ °C min}^{-1}$  to the desired temperature and held at each temperature for 2 minutes before data collection. A video showing a series of images from the in situ heating of a P3HT

thin film can be found in the supplementary information. A schematic of thin films with random, perpendicular, and parallel P3HT lamellae orientations is shown in **Scheme 1**. Upon heating, the P3HT (200) peak shifts to a lower  $q$ , indicating an increase in the P3HT layer spacing (**Figure 2a**). Upon cooling, the layer spacing decreases, but does not completely return to



**Scheme 1.** Cartoons of P3HT thin films with a) random, b) perpendicular, and c) parallel P3HT lamellae orientations relative to the substrate. The crystallographic directions are shown relative to the molecular structure in d). The P3HT layers lie in the (100) plane, the [100] direction is normal to the P3HT layers, the  $\pi$ -face lies in the (010) plane, the  $\pi$ - $\pi$  stacking direction is along the [010] direction, and the chain backbone is along the [001] direction.

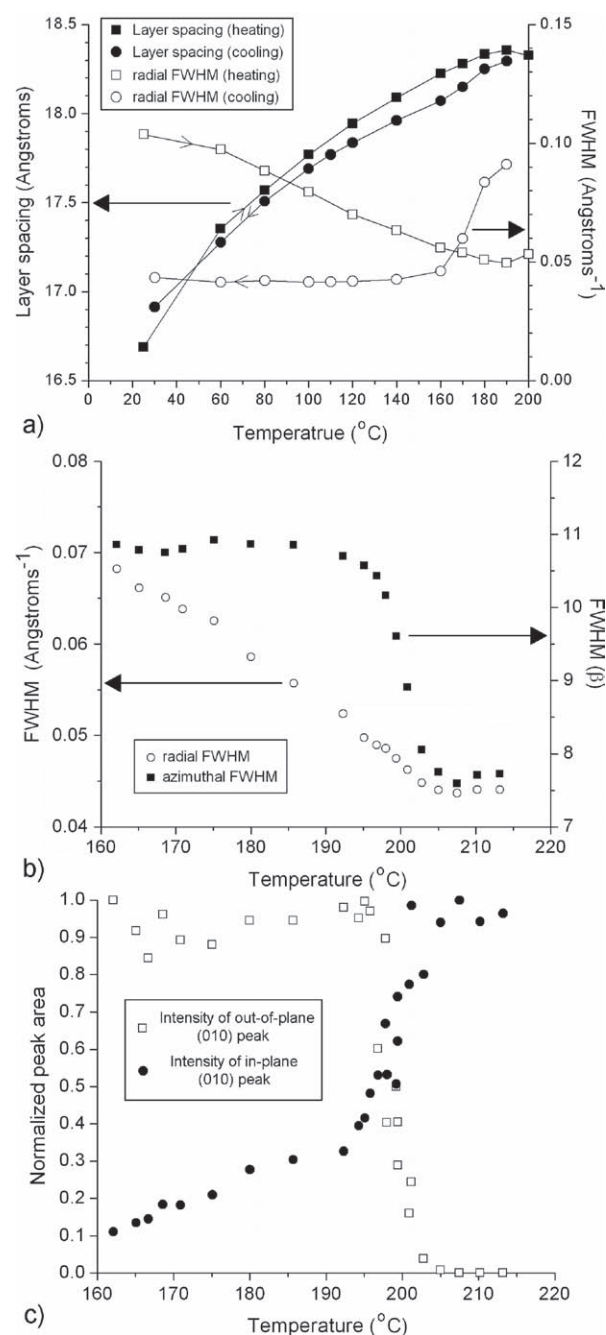


**Figure 2.** Thermal behavior of pure P3HT films. a) The P3HT layer spacing and radial FWHM (along  $q$ ) of the (200) peak are shown as a function of temperature for a P3HT thin film during in situ heating. No data are available for temperatures above 200 °C, as the peak disappears above the melting point. b) The FWHM of the (200) peak in the radial (along  $q$ ) and azimuthal (along  $\beta$ ) directions are shown as a function of temperature for P3HT thin films annealed with a thermal gradient. For the analysis of the (200) peak a cake slice was taken from  $q = 0.62 \text{ \AA}^{-1}$  to  $0.86 \text{ \AA}^{-1}$  and  $\beta = 60^\circ$  to  $120^\circ$ . c) The peak area for the out-of-plane (010) peak (cake slice of  $q = 1.45 \text{ \AA}^{-1}$  to  $1.85 \text{ \AA}^{-1}$  and  $\beta = 60^\circ$  to  $120^\circ$ ) and in the in-plane (010) peak (box from  $q_{xy} = 1.5 \text{ \AA}^{-1}$  to  $1.8 \text{ \AA}^{-1}$  and  $q_z = 0.03 \text{ \AA}^{-1}$  to  $0.40 \text{ \AA}^{-1}$ ) was measured as a function of temperature in the P3HT thin films annealed with a thermal gradient. Selected GIXS images and the regions selected for analysis are shown in Figure S1 and S2 of the supplementary information.



the original value from the as-cast film. Thermal expansion accounts for a majority of the initial layer spacing increase, and is reversible, as evidenced by the decrease in layer spacing upon cooling. However, there is also an irreversible process that occurs during annealing: improved ordering of the alkyl chains leads to a more extended conformation of the alkyl chains and a larger layer spacing after annealing.

In order to access the P3HT crystallite coherence length, the radial (along  $q$ ) full width at half maximum (FWHM) of the nominally out-of-plane (200) peak is used. The FWHM decreases upon heating, indicating an increase in the coherence length, until  $\sim 180^\circ\text{C}$  where the FWHM rapidly increases until the peak is no longer visible at  $205^\circ\text{C}$  (Figure 2a). The disappearance of the (100) peak and higher order reflections, including the (200) peak, indicates that the melting point of P3HT has been reached. Upon cooling the (100) and higher order reflections return, and the FWHM rapidly decreases upon cooling until  $\sim 140^\circ\text{C}$ , below which the FWHM remains constant. In Figure 1b a GIXS image of a P3HT thin film annealed at  $220^\circ\text{C}$  and subsequently cooled to room temperature is shown; in comparison with the as-cast film (Figure 1a), there is much stronger preferential orientation of the out-of-plane (100) peak, indicating an increase in the alignment of the P3HT lamellae parallel to the substrate.

A second out-of-plane peak, the (010), is present in the as-cast film at a  $q$  of  $\sim 1.65\text{ \AA}^{-1}$ : this corresponds to the  $\pi$ - $\pi$  stacking of the thiophene backbone. In the as-cast film the  $\pi$ - $\pi$  stacking direction is predominantly perpendicular to the substrate, with the  $\pi$ -face parallel to the substrate. It should be noted that there is evidence of some  $\pi$ - $\pi$  stacking parallel to the substrate, as indicated by the weak in-plane scattering at  $1.65\text{ \AA}^{-1}$ . Upon heating to the P3HT  $T_m$ , the (010) peaks disappear, indicating the complete loss of  $\pi$ - $\pi$  stacking order. Upon cooling only the in-plane (010) peak is observed, indicating that the  $\pi$ - $\pi$  stacking direction is now predominantly parallel to the substrate and the  $\pi$ -face perpendicular to the substrate (Figure 1b). This  $\pi$ - $\pi$  stacking orientation is consistent with the strong out-of-plane (100) peak observed in the annealed film. Annealing above the P3HT melting transition, and subsequent cooling, allows for the film-substrate system to achieve a lower free-energy state, resulting in an orientation of the P3HT lamellae and the  $\pi$ - $\pi$  stacking direction parallel to the substrate.

In order to investigate the effects of annealing at various temperatures upon the P3HT thin films in more detail, we used a thermal gradient annealing procedure across a P3HT thin film on a silicon wafer. The thermal gradient produced a range of temperatures from  $219.5^\circ\text{C}$  to  $161.7^\circ\text{C}$ . By taking a series of GIXS images at selected positions across the length of the substrate, we are able to rapidly and precisely investigate a range of annealing temperatures (see Figure S2 of the supplementary information for selected GIXS images near the P3HT  $T_m$ ). Note that the GIXS studies were on films cooled to ambient temperature. The uncertainty in the temperature due to the width of the beam is less than  $0.3^\circ\text{C}$ .

For P3HT films annealed below  $195^\circ\text{C}$  a decrease in the radial FWHM of the (200) peak is observed with increasing temperature, indicating an increase in the coherence length resulting from the annealing (Figure 2b). This corroborates the similar decrease in the radial FWHM of the (200) peak observed

in the in situ heating experiments as seen in Figure 2a. For films annealed below  $195^\circ\text{C}$  the intensity of the in-plane (010) peak slowly increases with temperature, indicating an increase  $\pi$ - $\pi$  stacking orientated parallel to the substrate. No change in the scattering intensity of the out-of-plane (010) peak, however, is observed for films annealed below  $195^\circ\text{C}$  (see Figure 2c). The decrease in the radial FWHM of the out-of-plane (200) peak and the increased intensity of the in-plane (010) peak indicates the growth of crystallites with P3HT lamellae oriented parallel to the substrate; while the unchanged intensity of the out-of-plane (010) peak indicates that there are no changes to the number of crystallites with  $\pi$ - $\pi$  stacking direction orientated perpendicular to the substrate. Thus it is concluded that annealing below  $195^\circ\text{C}$  leads to crystallite growth, most likely by consuming amorphous regions in the semicrystalline P3HT, but no overall re-orientation relative to the substrate.

In contrast, as the annealing temperature approaches the P3HT  $T_m$  ( $205^\circ\text{C}$ ) a dramatic re-orientation of the P3HT crystallites is observed. A sharp decrease in the azimuthal FWHM of the (200) peak along  $\beta^{[22-25]}$  occurs from  $195^\circ\text{C}$  to  $205^\circ\text{C}$  and the radial FWHM of the (200) peak steadily decreases until reaching a plateau (minimum) at  $205^\circ\text{C}$  (Figure 2b). These observations indicate, respectively, that the crystallites have developed a stronger (100) orientation relative to the substrate, and that the coherence length has increased. Similarly, as the annealing temperature is raised above  $195^\circ\text{C}$ , scattering from the out-of-plane (010) peak sharply decreases and completely disappears by  $205^\circ\text{C}$ , while the in-plane (010) peak reaches a maximum at the same temperature (Figure 2c). These results corroborate the in situ observation that the P3HT  $T_m = 205^\circ\text{C}$ , and they show that the re-orientation of the P3HT lamellae and of the  $\pi$ - $\pi$  stacking does not occur unless the film is cooled from the melt. Most likely, during crystallization from the melt, heterogeneous nucleation of P3HT crystallites occurs at the substrate interface<sup>[26]</sup> resulting in the strong orientation of the crystallites. This is in contrast to annealing of P3HT below the melting point, where existing crystallites grow but there is insufficient molecular mobility for re-orientation of existing crystallites.

In order to investigate the effects of thermal annealing on the surface morphology of the P3HT thin films, we probed the surface of the films annealed with a thermal gradient with atomic force microscopy (AFM). For each AFM image the root mean squared (RMS) roughness of the film was determined, and is shown as a function of annealing temperature in Figure 3 (The corresponding AFM images are shown in Figure S3). The as-cast film displays a roughness of  $0.36\text{ nm}$ . As the annealing temperature increases and approaches the P3HT  $T_m$  of  $205^\circ\text{C}$ , the RMS film roughness increases significantly. The increasingly textured surface morphology, upon annealing below the P3HT  $T_m$ , is due to the growth of existing crystallites at the expense of smaller crystallites or amorphous regions. This result is in agreement with the observed decrease in the radial FWHM of the (200) peak, which indicates an increase in the P3HT crystallite coherence length with increasing annealing temperature. The film annealed at  $203^\circ\text{C}$  displayed the maximum roughness,  $0.99\text{ nm}$ . However, when the annealing temperature is raised above the P3HT  $T_m$ , and the film crystallizes upon cooling through melt crystallization, the films display a

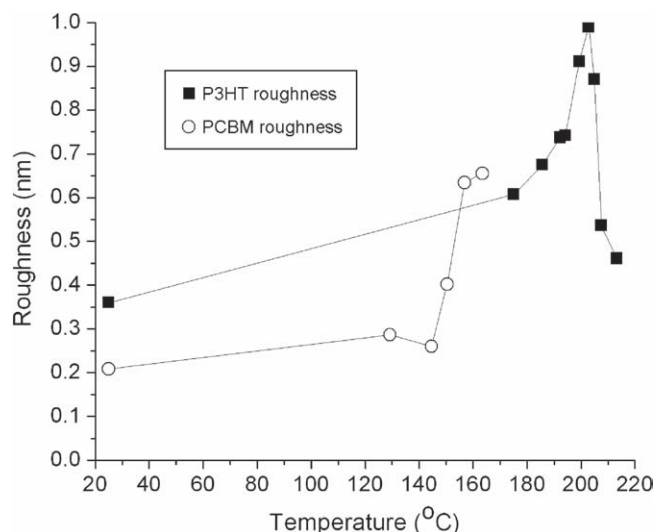


**Figure 3.** RMS roughness of P3HT (solid squares) and PCBM (open circles) thin films as a function of annealing temperature as determined from AFM scans. The corresponding AFM height images for each data point can be found in Figure S3 and S6 of the supplementary information.

markedly decreased roughness. Crystallization that occurs upon cooling from the melt takes place by heterogeneous nucleation of crystallites at the substrate interface and the crystallization front moves relatively uniformly through the thickness of the film consuming the amorphous regions. Thus, melt crystallization results in a relatively smooth film. This substrate-induced nucleation hypothesis is supported by the observation of oriented P3HT crystallites for films annealed above the P3HT  $T_m$ . This is in contrast to the roughness induced upon annealing below the  $T_m$ , where existing crystallites grow at the expense of smaller crystallites and amorphous regions and are not able to preferentially orient with respect to the substrate.

Several groups have reported the formation of P3HT nanofibrils in thin films. These structures are enhanced for films that have been thermally annealed,<sup>[27,28]</sup> drop cast,<sup>[28–30]</sup> or cast from high boiling-point solvents.<sup>[31,32]</sup> These nanofibril structures are typically observed in low molecular weight polythiophenes (<20,000 g mol<sup>−1</sup>) and not in higher molecular weight counterparts.<sup>[33–35]</sup> In the present study the P3HT molecular weight was a high 50 000 g mol<sup>−1</sup> and, as expected, nanofibrils were not observed in the films investigated here.

In this section we have demonstrated the utility of both in situ heating and thermal gradient annealing for the morphological characterization of P3HT thin films both during the thermal annealing process and after thermal annealing. The as-cast P3HT displays crystallites that have a  $\pi$ – $\pi$  stacking direction primarily perpendicular to the substrate (i.e., with the  $\pi$ -face parallel to the substrate). GIXS during in situ heating revealed an increase in the P3HT layer spacing and the crystallite coherence length with increasing temperature until approaching the melting point, observed at 205 °C. Characterization of P3HT thin films annealed with a thermal gradient (and subsequently cooled to room temperature) suggest two distinct crystallization mechanisms that occur for annealing above and below the P3HT  $T_m$ . GIXS and AFM reveal that with increasing annealing

temperature, until the P3HT  $T_m$ , the coherence length of the P3HT crystallites and the surface roughness of the films increase, indicating growth of the existing P3HT crystallites. When the annealing temperature is above the P3HT  $T_m$  a dramatic re-orientation of the P3HT crystallites is observed: the P3HT lamellae and the  $\pi$ – $\pi$  stacking direction are preferentially oriented parallel to the substrate. The orientation observed is a result of heterogeneous nucleation at the substrate interface upon cooling from the melt. These melt-crystallized P3HT films are relatively smooth compared to the films annealed below the P3HT  $T_m$ .

## 2.2. Thermal Annealing of PCBM Thin Films

In situ thermal annealing GIXS measurements were performed on spin cast PCBM films with thicknesses of 20 to 25 nm. In the as-cast film there are isotropic rings visible at  $q \approx 0.71 \text{ \AA}^{-1}$ ,  $1.39 \text{ \AA}^{-1}$ , and  $2.04 \text{ \AA}^{-1}$  (Figure 1i). The breadth of these rings in the radial direction indicates that the PCBM is amorphous or consists of very small crystallites. Upon heating the PCBM films directly to 205 °C the formation of several distinct peaks from the isotropic rings is observed. The appearance of these peaks indicates the crystallization of PCBM below the melting temperature, i.e. cold crystallization. Further heating results in a decrease in intensity of these peaks, until eventually at 300 °C all of the peaks have disappeared, indicating complete melting of the PCBM crystallites. The same crystalline peaks return upon cooling, due to melt crystallization, at roughly the same temperatures at which they disappear upon heating; see Figure 1j for a GIXS image of the annealed PCBM film. A video showing a series of images from the in situ heating of a PCBM thin film can be found in the supplementary information. We have not identified the exact structure of the PCBM crystallites in these films; this topic is beyond the scope of this paper.

To determine the precise temperature at which cold crystallization occurs, we investigated a PCBM thin film annealed with a thermal gradient. By integrating the intensity of the peak located from  $q = 1.27$  to  $1.65 \text{ \AA}^{-1}$  and  $\beta = 60$  to  $68^\circ$ , and subtracting the background scattering, we obtained a quantitative assessment of the annealing-induced relative degree of crystallinity. The region selected for analysis is shown in Figure S4 of the supplementary information. Figure 4a shows a plot of this integrated intensity as a function of annealing temperature, and Figure S2 of the supplementary information shows selected GIXS images near the PCBM cold-crystallization temperature. The first observation of scattering from the PCBM crystallites above the background appears at 142 °C and the intensity continues to increase until 155 °C, above which the peak intensity does not significantly change with increasing annealing temperature. In contrast to the increase in the coherence length of P3HT crystallites, which occurs over a broad annealing temperature range, the annealing temperature above which cold crystallization of PCBM occurs, 142 °C to 155 °C, is very sharp. The increased molecular mobility that allows for the cold crystallization of PCBM indicates that the glass transition temperature ( $T_g$ ) of PCBM has been reached.<sup>[36]</sup>

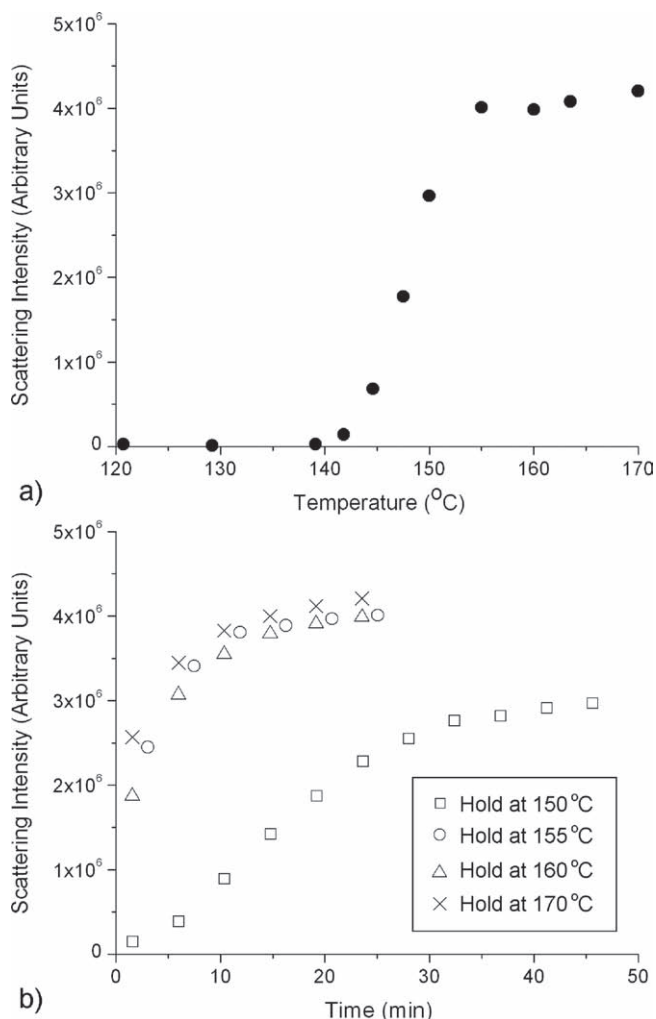


**Figure 4.** a) PCBM films were annealed by applying a thermal gradient across the length of a silicon wafer in order to achieve a range of thermal annealing temperatures across a single thin film. b) In situ GIXS measurements were taken as each film was held at the specified temperature. Selected GIXS images and the regions selected for analysis are shown in Figure S2 and S4 of the supplementary information. The normalized data and the model fits for each temperature are shown in Figure S5 in the supplementary information.

It is important to note that distinct peaks, and not an isotropic ring, indicate that the crystallites are preferentially oriented relative to the substrate, suggesting heterogeneous nucleation at the substrate interface.

In order to gain insight into the kinetics of the cold-crystallization process, we performed a series of in situ heating experiments where the PCBM thin film was heated to a particular temperature and the development of the crystallites was monitored as a function of time. The appearance of the crystalline peaks can be observed in the video of a PCBM thin film held at 150 °C for 45 min, available in the supplementary information. Figure 4b shows a plot of the relative crystallinity (integrated intensity) as a function of time for thin films that were heated to 150 °C, 155 °C, 160 °C, or 170 °C, and held there for 25 to 45 min. The increase

in the relative crystallinity follows the form of the Avrami equation:<sup>[37–39]</sup>

$$1 - X(t) = (1 - A) * [\exp(-K * t^n)]$$

where  $X(t)$  is the fractional crystallinity at time  $t$ ;  $A$  represents the initial fraction of crystallization that has taken place when the desired temperature has been reached ( $t = 0$ );  $K$  represents the overall crystallization rate constant, and  $n$  is the Avrami exponent, which depends both on the nature of nucleation and on the growth geometry. Table 1 shows the values for the Avrami parameters  $A$ ,  $K$ , and  $n$  as a function of the PCBM cold-crystallization temperature. For the fit, the calculated Pearson correlation coefficients,  $R^2$ , were 0.99932, 0.99881, 0.99906, and 0.99883 for 150 °C, 155 °C, 160 °C, and 170 °C, respectively, indicating a very good agreement between the model and experiment.

The fractional crystallinity  $X(t)$  for each data set is determined by normalizing the background-subtracted integrated intensity of the crystalline PCBM peak (located from  $q = 1.27$  to  $1.65 \text{ \AA}^{-1}$  and  $\beta = 60$  to  $68^\circ$ ) relative to the final image taken at the given temperature. The normalized data and the model fits for each temperature are shown in Figure S5 in the supplementary information. The parameter  $A$  increases as the annealing temperature is increased, indicating that more crystallization occurs before  $t = 0$  for the higher hold temperatures. As the temperature ramp rate is  $2 \text{ }^\circ\text{C min}^{-1}$ , the films spend significant time above the cold-crystallization temperature before the hold temperature is reached, leading to the observed crystallization before the so-called “ $t = 0$ ”. The Avrami analysis reveals different growth mechanisms for films annealed at 150 °C compared to the films annealed at 155 °C, 160 °C, and 170 °C. The values of  $K$  and  $n$  are identical within the margin of error (averages of  $K = 0.20$  and  $n = 0.98$ ) for the cold crystallization taking place at 155 °C, 160 °C, and 170 °C. The overall crystallization rate constant,  $K$ , is significantly lower for the PCBM film annealed at 150 °C ( $K = 0.004$ ). This increase in the overall crystallization rate at 155–170 °C is a result of the increased mobility associated with the PCBM  $T_g$ .

An Avrami exponent of  $n \approx 1$  observed for cold crystallization occurring at 155 °C, 160 °C, and 170 °C indicates one-dimensional crystallite growth with heterogeneous nucleation at the substrate,<sup>[39]</sup> resulting in a strong preferential orientation of the crystallites. The formation of distinct peaks and not isotropic rings supports this conclusion and since the film temperature is above the PCBM  $T_g$ , nucleation is rapid. The high density of nucleation sites at the interface limits the growth to one dimension, i.e. perpendicular to the substrate, as the growing grains impinge upon each other in the plane of the substrate in the

**Table 1.** The Avrami parameters for each PCBM cold crystallization temperature.

Temperature [°C]	$A$	$K$	$n$
150	$0.03 \pm 0.01$	$0.004 \pm 0.001$	$1.83 \pm 0.07$
155	$0.22 \pm 0.15$	$0.24 \pm 0.11$	$0.96 \pm 0.16$
160	$0.28 \pm 0.05$	$0.20 \pm 0.05$	$0.97 \pm 0.09$
170	$0.49 \pm 0.03$	$0.17 \pm 0.04$	$1.00 \pm 0.09$

very initial stages of crystallization. The initial crystallization stages are not captured in these experiments, as the first GIXS measurement takes place after the crystallite growth has been limited to one dimension. For cold crystallization occurring at 150 °C, the Avrami exponent  $n$  is 1.83, indicating heterogeneous nucleation with crystallite growth of a higher dimensionality.<sup>[39,40]</sup> At this temperature, essentially the  $T_g$ , only the lowest energy sites are able to nucleate crystallites. As fewer sites for crystallization are available, the grains do not impinge upon each other in the early stages of growth and are free to grow in two or three dimensions. Pure 1D, 2D, and 3D growth would exhibit Avrami exponents of 1, 2, and 3, respectively: the Avrami exponent of 1.83 most likely indicates a combination of 1D, 2D, and 3D growths, with the substrate and some crystallite impingement limiting the growth from becoming completely three dimensional. A cartoon illustrating crystallite growth with dimensionalities of 1.8 and 1 resulting from low- and high-density nucleation, respectively, is shown in **Scheme 2**.

The surface morphology of the PCBM thin films annealed at various temperatures was investigated with AFM, and the RMS

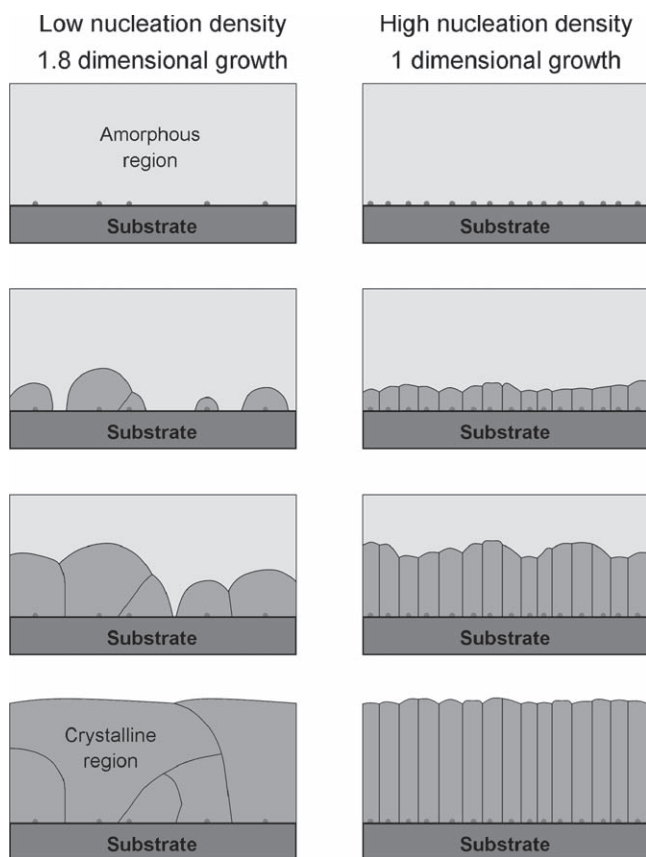
roughness as a function of annealing temperature is shown in Figure 3 (The corresponding AFM images are shown in Figure S6). The as-cast film displays a roughness of 0.21 nm; as the annealing temperature is raised above the cold crystallization temperature, a sharp increase in the film roughness is observed. The increase in surface roughness directly coincides with the observation of cold crystallization in GIXS of the same films. The growth of PCBM crystallites through cold crystallization results in an increasingly textured film, similar to the roughness observed due to the growth of P3HT crystallites below the  $T_m$ . However, no further increase in roughness is observed for PCBM films annealed above 155 °C. The cold crystallization of PCBM occurs through the same growth mechanism for annealing temperatures above 155 °C – as indicated by the in situ GIXS heating measurements – resulting in the similar thin film surface morphologies.

In this section we have observed the cold crystallization of amorphous PCBM thin films annealed above the glass transition temperature. GIXS and AFM reveal that the scattering intensity from PCBM crystallites and the surface roughness both increase sharply as the annealing temperature is increased above 142 °C, until a plateau is reached at 155 °C. In situ GIXS characterization of PCBM films above the  $T_g$  provides a quantitative measurement of the fraction of crystallization as a function of time and allows for determination of the crystallization mechanisms. Using the Avrami equation we were able to determine that PCBM cold crystallization occurs through heterogeneous nucleation at the substrate, and for temperatures above 155 °C the growth is limited to one dimension due to impingement of neighboring crystallites in the plane of the substrate. This knowledge of the PCBM crystallization mechanisms can be used to manipulate the PCBM crystallinity and in turn phase segregation induced by domain coarsening as a function of annealing temperature.

### 2.3. Thermal Annealing of P3HT–PCBM Blend Thin Films

In order to observe the behavior of the individual components when incorporated into a bulk heterojunction, we investigated thin films of P3HT–PCBM blends with ratios of 3:1, 1:1, and 1:3 (75% P3HT–25% PCBM, 50% P3HT–50% PCBM, and 25% P3HT–75% PCBM, respectively, with all compositions quoted as weight percents). GIXS of the as-cast films of the blends reveals a superposition of the scattering features of the P3HT and the PCBM as a result of phase separation. Each blend displays features of each component, with scattering intensities roughly corresponding to the relative concentrations of the components (Figure 1c, 1e, and 1g).

In the as-cast 3:1 blend (Figure 1c) the same features are observed as in the pure P3HT thin film, with the addition of an isotropic ring at  $q \approx 1.39 \text{ \AA}^{-1}$  resulting from the amorphous PCBM. After annealing, the P3HT in the 3:1 blend (Figure 1d) has fully re-oriented with the P3HT lamellae and the  $\pi$ – $\pi$  stacking direction parallel to the substrate in the same manner as pure P3HT. In order to precisely determine the temperature at which the re-orientation of P3HT occurs, we again used GIXS to investigate a thin film that had been annealed with a thermal gradient. The disappearance of the out-of-plane



**Scheme 2.** Cartoons illustrating PCBM crystallite growth for: low density nucleation and subsequent crystallite growth with a dimensionality of  $\sim 1.8$ , as observed for cold crystallization taking place at 150 °C (left); and high density nucleation and subsequent crystallite growth with a dimensionality of  $\sim 1$ , as observed for cold crystallization taking place above 155 °C (right). The dots on the substrate represent nucleation sites, the light grey regions represent amorphous PCBM, and the medium grey regions represent PCBM crystallites. Schematic representation is not to scale for clarity.



**Table 2.** The P3HT melting temperature ( $T_m$ ) and PCBM glass transition temperature ( $T_g$ ) for each blend composition, determined from the analysis of the films annealed with a thermal gradient.

	P3HT $T_m$ [°C], re-orientation[a]	PCBM $T_g$ [°C], cold crystallization[b]
P3HT	205	-
3:1	201	-
1:1	195	103–119
3:1	-	117
PCBM	-	148

[a] The P3HT  $T_m$  was identified by the re-orientation of the P3HT (010) peak; when the integrated intensity of this peak reached the background the P3HT has fully re-oriented. [b] The PCBM  $T_g$  was identified by the half maximum of the PCBM peak intensity that arises during cold crystallization. A precise PCBM  $T_g$  could not be calculated for the 1:1 blend due to weak scattering from the crystalline PCBM. See Figure S2 in the supporting information for selected images used for transition temperature calculations. All of these values are in agreement with the data from in situ heating, however, precise values could not be extracted from the in situ heating measurements due to the coarse temperature steps between measurements.

scattering at  $q \approx 1.65 \text{ \AA}^{-1}$  (from the P3HT  $\pi$ - $\pi$  stacking) occurs at 201 °C, a slightly lower temperature than in the pure P3HT thin film (see Figure S2). Hence, the melting temperature of the P3HT within the 3:1 blend is lower than the pure P3HT by about 4 °C. The transition temperatures observed for each blend are shown in Table 2. There is no evidence of PCBM crystallization in the 3:1 blend thin films. The as-cast 1:1 P3HT – PCBM blend shows the same features as the as-cast 3:1 blend, but with a further increase in the intensity of the isotropic ring at  $q \approx 1.39 \text{ \AA}^{-1}$  from the amorphous PCBM and a decrease in intensity of the scattering from the P3HT crystallites (Figure 1e). Annealing of the 1:1 blend thin film once again results in the re-orientation of the P3HT lamellae parallel to the substrate (Figure 1f). GIXS of a 1:1 film annealed with a thermal gradient reveals that full P3HT crystallographic re-orientation occurs for films annealed above 195 °C (see Figure S2). The systematic decrease in the P3HT re-orientation temperature indicates that the presence of PCBM in the blend reduces the P3HT melting temperature. There is some evidence of PCBM crystallization: several weak peaks are visible at  $q \approx 1.39 \text{ \AA}^{-1}$ , beginning at temperatures around 103–119 °C. However, the precise temperature of the onset of PCBM crystallization could not be determined due to a low scattering signal from the PCBM crystallites. The lack of distinct peaks from the crystalline PCBM in the 1:1 blend is most likely due to the small crystallite size and the lack of preferential orientation relative to the substrate.

In situ heating measurements of 3:1 and 1:1 blends reveal a decrease in the P3HT melting temperature – disappearance of the (200) and (010) peaks – with increasing PCBM content; corroborating the decrease in the P3HT re-orientation temperatures with increasing PCBM content observed in the films annealed with a thermal gradient. The P3HT layer spacing and radial FWHM of the (200) peak for the 3:1 and 1:1 blends during in situ heating and cooling are shown in Figure 5; both blends display similar behavior to the pure P3HT thin film. Inspection of the data from the in situ heating of P3HT, the 3:1 blend, and the 1:1 blend thin films (Figure 2a, 5a, and 5b, respectively) reveals that the radial FWHM is larger

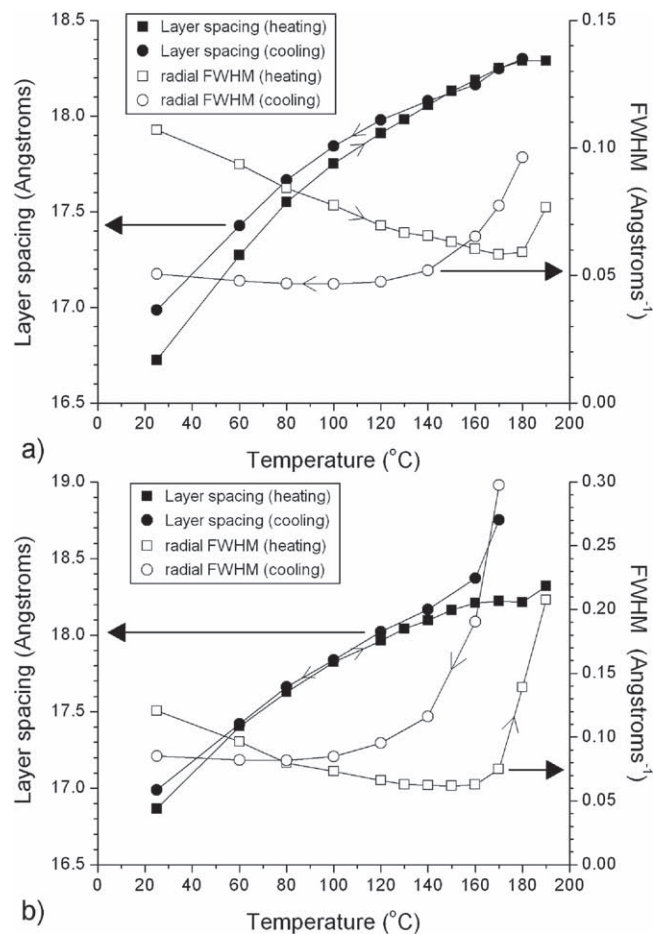


**Figure 5.** The P3HT layer spacing and radial FWHM are shown as a function of temperature for a) 3:1 P3HT–PCBM blend and b) 1:1 P3HT–PCBM blend thin films during in situ heating. Radial integration of a cake slice was taken from  $q = 0.62 \text{ \AA}^{-1}$  to  $0.86 \text{ \AA}^{-1}$  and  $\chi = 60^\circ$  to  $120^\circ$ , the P3HT (200) peak was used for determination of the layer spacing and the radial FWHM. No data are available for temperatures above 190 °C, as the peak disappears above the melting point.

throughout the heating and cooling cycle for blends with increasing PCBM content. The values of the layer spacing and the radial FWHM of the P3HT (200) peak are shown for the as-cast and films annealed at 220 °C in Table 3: both before and after annealing the layer spacing and radial FWHM monotonically increases as the PCBM content is increased. This increase in the radial FWHM indicates that PCBM restricts the crystallization of P3HT, limiting the crystallite size. It is well known that the melting temperature of semi-crystalline polymers is sensitive to the size of the crystallites, where the melting temperature is reduced for smaller crystallites.<sup>[41]</sup> Thus it is concluded that the inclusion of PCBM in the as-cast blend disrupts the crystallization of P3HT, reducing the crystallite size and thus the melting temperature of the blend films. Presumably, if large-scale phase separation were to take place upon extended thermal annealing at temperatures above the P3HT  $T_m$ , the PCBM would no longer have an effect on this value.



**Table 3.** The P3HT layer spacing and the radial (along  $q$ ) FWHM for as-cast and annealed P3HT, 3:1 blend, and 1:1 blend thin films.

	As-cast		Annealed at 220 °C	
	Layer spacing [nm]	FWHM [ $\text{\AA}^{-1}$ ]	Layer spacing [nm]	FWHM [ $\text{\AA}^{-1}$ ]
P3HT	16.68	0.103	16.91	0.043
3:1	16.72	0.107	16.99	0.051
1:1	16.86	0.121	16.99	0.085

AFM of the 3:1 and 1:1 blend thin films reveals similar surface morphology behavior as the pure P3HT thin films. The film roughness increases with increasing annealing temperature until the melting temperature of P3HT is reached. This increase in roughness again corresponds to an increase in the coherence length of the P3HT crystallites. Similar to the pure P3HT thin films, when the annealing temperature of the 3:1 and 1:1 blend thin films is raised above the P3HT  $T_m$ , a decrease in roughness is observed. It is not surprising that the blend films show the same surface morphology as the pure P3HT film: it has been shown that the P3HT preferentially phase segregates to the air interface,<sup>[13,42,43]</sup> thus the PCBM component would not be expected to significantly affect the surface morphology of the blends.

In the as-cast 1:3 P3HT – PCBM thin film the P3HT (100) peak and higher order reflections are not clearly visible, suggesting that the P3HT has not formed distinct crystalline domains (Figure 1g). This is in contrast to the 3:1 and 1:1 blends where crystalline P3HT is observed. Upon annealing the 1:3 P3HT – PCBM blend significant crystallization of P3HT and PCBM is seen (Figure 1h). GIXS of a 1:3 blend thin film annealed with a thermal gradient revealed that films annealed above 113 °C display signs of PCBM crystallinity, indicating a reduction in the PCBM  $T_g$ ; selected GIXS images above and below 113 °C are shown in Figure S2 of the supplementary information. The presence of P3HT reduces the  $T_g$  of the blend,<sup>[18]</sup> allowing PCBM cold crystallization to occur at a lower temperature than in the pure PCBM film. PCBM cold crystallization within the P3HT–PCBM blend results in phase segregation, due to the exclusion of P3HT from the PCBM crystallite domains.<sup>[11,13,17,21]</sup> The scattering peaks from the PCBM component in the annealed 1:3 blend film are both radially (along  $q$ ) and angularly (along  $\beta$ ) broader compared to those from the pure PCBM. It appears that the presence of P3HT in the 1:3 blends is restricting the PCBM crystallization to smaller crystallites with less orientation relative to the substrate, resulting in the peak broadening along  $q$  and  $\beta$ , respectively. The details of the PCBM crystal structure<sup>[44–45]</sup> are beyond the scope of this paper. Optical microscopy of 1:3 blend films annealed above 113 °C reveals islands  $\sim 5 \times 1 \mu\text{m}$  in size that develop as a result of de-wetting (Figure S7a). Profilometry confirms the presence of the islands which are  $\sim 100$  nm in height. This result indicates that there is the ability for large scale molecular rearrangement in both components above the cold-crystallization temperature of PCBM. The films that display de-wetting are only 20 to 25 nm thick; de-wetting does not occur in thicker films, which was confirmed by annealing a 75 nm thick 1:3 blend film at 160 °C (Figure S7b).

It should be noted that the transition temperatures reported here are consistently lower than those reported by others in the literature. Other studies of the thermal phase behavior of P3HT–PCBM blends have utilized DSC or optical microscopy,<sup>[17]</sup> where the blends studied are either in the bulk or are films with crystallites several microns in size. The films investigated in this study were 20 to 25 nm, which limits the crystallite size, resulting in the lower transition temperatures observed in this study.

We have shown that the PCBM  $T_g$  and the P3HT  $T_m$  vary as a function of blend ratio and annealing above these transition temperatures results in significant morphological rearrangements. It is desirable to increase crystallinity (increasing the charge-carrier mobility) within each domain, without allowing excessive domain coarsening, which would increase exciton recombination. As the morphological evolution as a function of annealing conditions is altered by changes in the blend composition, the optimal annealing conditions for BHJ solar cell devices will also depend on blend composition. Thus, an understanding of how to utilize thermal annealing to control crystallite growth and orientation is important for the optimization of processing conditions for solar cell device fabrication.

### 3. Conclusions

In summary, we have systematically characterized the thin film behavior of P3HT, PCBM, and BHJ blends of the two components with GIXS both during the thermal annealing process (in situ heating) and after thermal annealing (films annealed with a thermal gradient) up to 220 °C.

The as-cast P3HT thin films display crystallites that have  $\pi$ – $\pi$  stacking primarily perpendicular to the substrate (the  $\pi$ -face parallel to the substrate). GIXS during in situ heating revealed an increase in the P3HT layer spacing and the coherence length of the crystallites with increasing temperature, until approaching the melting point, observed at 205 °C. GIXS and AFM of P3HT thin films annealed with a thermal gradient (and subsequently cooled to room temperature) suggest two distinct crystallization mechanisms that occur for annealing above and below the P3HT  $T_m$ . As the annealing temperature is increased up to the P3HT  $T_m$ , existing P3HT crystallites grow with increasing annealing temperatures. In contrast, upon cooling the P3HT films from the melt (after annealing above the P3HT  $T_m$ ), heterogeneous nucleation at the substrate interface results in a re-orientation of the P3HT crystallites. The melt-crystallized P3HT has the P3HT lamellae and the  $\pi$ – $\pi$  stacking direction preferentially oriented parallel to the substrate.

Annealing of amorphous PCBM thin films above the glass transition temperature results in cold crystallization, as evidenced by the appearance of crystalline diffraction peaks and an increased surface roughness. In situ GIXS characterization of PCBM films above the  $T_g$  provides a quantitative measurement of the fraction of crystallization as a function of time and allows for the determination of crystallization mechanisms. Using the Avrami equation we were able to determine that PCBM cold crystallization occurs through heterogeneous nucleation at the substrate, and for temperatures above 155 °C the growth is

limited to one dimension due to impingement of neighboring crystallites in the plane of the substrate.

By applying the same characterization techniques to a series of P3HT–PCBM bulk heterojunction blends, we were able to investigate the effects of incorporating each component into a BHJ blend as a function of blend composition and annealing temperature. The P3HT component in the 3:1 and 1:1 P3HT–PCBM blends displays similar behavior as the pure P3HT film: growth of existing crystallites for films annealed below the  $T_m$  and a reorientation of the P3HT crystallites due to heterogeneous nucleation at the substrate interface when cooled from the melt. However, increasing PCBM content leads to a reduction in the P3HT crystallite size and a corresponding reduction in the P3HT melting point. Similarly, a reduction in the PCBM  $T_g$  is observed with increasing P3HT content for the 1:3 and 1:1 blend films.

Understanding how various annealing conditions affect morphology of polymer – fullerene BHJ blends is critical for the design and optimization of systems for use in high-performance solar cell devices. This work provides insights into the nature of the crystallization processes of both P3HT and PCBM as pure components and in BHJ blends, and illustrates the need to understand the thermal phase behavior of each component as a function of blend composition. The techniques demonstrated in this work can be implemented to identify key transition temperatures for new polymer–fullerene blend combinations, thus guiding the optimization of the processing conditions for solar cell device fabrication.

## 4. Experimental Section

Poly(3-hexylthiophene) (P3HT) with a molecular weight of  $\sim 50,000$  g mol $^{-1}$  and  $\sim 95\%$  regioregular, was purchased from Rieke Metals Inc. Phenyl-C61-butyric acid methyl ester (PCBM) was purchased from Nano-C. Chloroform was purchased from Sigma Aldrich. Five solutions were prepared: P3HT (2.0 mg mL $^{-1}$ ), P3HT (1.5 mg mL $^{-1}$ ) + PCBM (0.5 mg mL $^{-1}$ ), P3HT (1.0 mg mL $^{-1}$ ) + PCBM (1.0 mg mL $^{-1}$ ), P3HT (0.5 mg mL $^{-1}$ ) + PCBM (1.5 mg mL $^{-1}$ ), and PCBM (2.0 mg mL $^{-1}$ ), each in chloroform. Silicon wafers were cut ( $\sim 20$  mm  $\times$  20 mm) and rinsed with deionized water, toluene, acetone, and isopropyl alcohol, followed by a 15 minute oxygen plasma etch. The solutions were spin cast onto silicon wafers at 400 rpm for 10 seconds followed by 1000 rpm for 60 seconds and let dry overnight in a nitrogen glovebox. The film thicknesses were measured using a Veeco Dektak Stylus Profilometer with a tip radius of 12.5  $\mu$ m.

In the thermal gradient studies, two sets of films for each blend ratio were thermally annealed by positioning the substrate on a hotplate to create a silicon fin with an effective length of 50.5 mm with a nominal surface temperature of either 240 °C or 300 °C and an ambient temperature  $T_\infty$  of 27.5 °C, which is assumed to be constant. The substrates were annealed for 45 min at this temperature at which point the hotplate surface temperature was cooled at an approximate rate of 2 °C min $^{-1}$  for 120 min. Surface temperatures of the substrate were measured at specific points using a digital thermometer. The surface temperature profile was interpolated by modeling the silicon substrate as a fin with the convective heat flux at the tip. The heat transfer coefficient  $h$  was fitted using a least-squares method with the following material properties and geometry: heat conduction coefficient,  $k = 89.65$  W m $^{-2}$  K $^{-1}$ , fin width,  $w = 25.4$  mm, fin thickness,  $t = 0.65$  mm. The thermal gradient produced a range of  $T_s$  from 219.5 °C to 91.7 °C. The temperature profile for each gradient is shown in Figure S8 of the supplementary information. The uncertainty in the

sample temperature due to the width of the X-ray beam is less than 0.3 °C.

Atomic force microscopy topography images were acquired in the tapping mode regime using a Multimode AFM (Veeco). The surface roughness was measured from at least three different areas of the topography image.

Grazing incidence X-ray scattering (GIXS) measurements were performed at the Stanford Synchrotron Radiation Lightsources (SSRL) using beamline 11–3 with a photon wavelength of 0.09758 nm. The scattering intensity was detected on a 2-D image plate (MAR-345) with a pixel size of 150  $\mu$ m (2300  $\times$  2300 pixels) and analyzed using the software package WxDiff, provided by Dr. Stefan Mannsfeld. The samples were  $\sim 20$  mm long in the direction of the beampath, and the detector was located at a distance of 402.9 mm from the sample center. The incidence angle was chosen in the range of 0.10°–0.12° to optimize the signal to-background ratio. The beam size was 50  $\mu$ m  $\times$  150  $\mu$ m, which resulted in a beam footprint on sample 150  $\mu$ m wide over the entire length of the 20 mm long sample. The data were distortion-corrected ( $\theta$ -dependent image distortion introduced by planar detector surface) before performing quantitative analysis on the images. The overall resolution in the GIXD experiments, dominated by the sample size, was about 0.08 Å $^{-1}$ .

A custom built chamber and sample stage used for in situ heating experiments, see Figure S9 of the supplementary information, a substrate heater (model # 101126) was purchased from HeatWave Labs and mounted to the aluminum sample stage. A Watlow series 96 temperature controller was used to measure the temperature and apply the appropriate voltage to the heater. The sample stage was enclosed in an aluminum chamber with a  $\sim 200$  cm $^3$  min $^{-1}$  flow of helium into the chamber to reduce the background from air scattering and to prevent degradation of the sample at elevated temperatures. For all in situ heating measurements an initial GIXS image was taken at room temperature before any thermal treatment. The films were then heated at a rate of 10 °C min $^{-1}$  to the desired temperature and allowed to equilibrate at each temperature for 2 min before the collection of data. There is a 3 °C uncertainty in the film temperature due to temperature variations as a function of position on the film and temperature fluctuations as a function of time. Collection times ranges from 120 s to 180 s depending on the scattering strength of the films.

## Supporting Information

Supporting Information is available from the Wiley Online Library or from the author.

## Acknowledgements

This publication was partially based on work supported by the Center for Advanced Molecular Photovoltaics, Award No KUS-C1–015-21, made by King Abdullah University of Science and Technology (KAUST). We also acknowledge support from the Global Climate and Energy Program (GCEP) and the Stanford Center for Polymer Interfaces and Macromolecular Assemblies (CPIMA). EV would like to thank the Eastman Kodak Corporation and the Kodak Fellows Program for support. CJB was funded by a Ruth L. Kirschstein NIH fellowship (Grant #1F32NS064771–01). Portions of this research were carried out at the Stanford Synchrotron Radiation Lightsources, a national user facility operated by Stanford University on behalf of the U.S. Department of Energy, Office of Basic Energy Sciences. The authors would like to thank Stefan Mansfeld for providing the WxDiff software package for GIXS data analysis.

Received: May 16, 2010  
Published online: August 18, 2010

- [1] C. J. Brabec, J. R. Durrant, *MRS Bull.* **2008**, *33*, 670.
- [2] H. Hoppe, N. S. Sariciftci, *J. Mater. Chem.* **2006**, *16*, 45.
- [3] B. C. Thompson, J. M. J. Fréchet, *Angew. Chem. Int. Ed.* **2008**, *47*, 58.
- [4] X. Yang, J. Loos, *Macromolecules* **2007**, *40*, 1353.
- [5] S. Bertho, G. Janssen, T. J. Cleij, B. Conings, W. Moons, A. Gadisa, J. D'Haen, E. Goovaerts, L. Lutsen, J. Manca, D. Vanderzande, *Sol. Energy Mater. Sol. Cells* **2008**, *92*, 753.
- [6] G. Li, V. Shrotriya, J. S. Huang, Y. Yao, T. Moriarty, K. Emery, Y. Yang, *Nat. Mater.* **2005**, *4*, 864.
- [7] W. L. Ma, C. Y. Yang, X. Gong, K. Lee, A. J. Heeger, *Adv. Funct. Mater.* **2005**, *15*, 1617.
- [8] T. J. Savenije, J. E. Kroeze, X. N. Yang, J. Loos, *Adv. Funct. Mater.* **2005**, *15*, 1260.
- [9] F. Padinger, R. S. Rittberger, N. S. Sariciftci, *Adv. Funct. Mater.* **2003**, *13*, 85.
- [10] G. Li, Y. Yao, H. Yang, V. Shrotriya, G. Yang, Y. Yang, *Adv. Funct. Mater.* **2007**, *17*, 1636.
- [11] S. Miller, G. Fanchini, Y. Y. Lin, C. Li, C. W. Chen, W. F. Su, M. Chhowalla, *J. Mater. Chem.* **2008**, *18*, 306.
- [12] S. Cook, A. Furube, R. Katoh, *Jpn. J. Appl. Phys.* **2008**, *47*, 1238.
- [13] Y. Yao, J. H. Hou, Z. Xu, G. Li, Y. Yang, *Adv. Funct. Mater.* **2008**, *18*, 1783.
- [14] Z. Bao, A. Dodabalapur, A. J. Lovinger, *Appl. Phys. Lett.* **1996**, *69*, 4108.
- [15] H. Sirringhaus, P. J. Brown, R. H. Friend, M. M. Nielsen, K. Bechgaard, B. M. W. Langeveld-Voss, A. J. H. Spiering, R. A. J. Janssen, E. W. Meijer, P. Herwig, D. M. de Leeuw, *Nature* **1999**, *401*, 685.
- [16] J. Y. Kim, D. Frisbie, *J. Phys. Chem. C* **2008**, *112*, 17726.
- [17] C. Müller, T. A. M. Ferenczi, M. Campoy-Quiles, J. M. Frost, D. D. C. Bradley, P. Smith, N. Stingelin-Stutzmann, J. Nelson, *Adv. Mater.* **2008**, *20*, 3510.
- [18] J. Zhao, A. Swinnen, G. Van Assche, J. Manca, D. Vanderzande, B. Van Mele, *J. Phys. Chem. B* **2009**, *113*, 1587.
- [19] M. Y. Chiu, U. S. Jeng, M. S. Su, K. H. Wei, *Macromolecules* **2010**, *43*, 428.
- [20] Y. Kim, S. Cook, S. M. Tuladhar, S. A. Choulis, J. Nelson, J. R. Durrant, D. D. C. Bradley, M. Giles, I. McCulloch, C. S. Ha, M. Ree, *Nat. Mater.* **2006**, *5*, 197.
- [21] C. H. Woo, B. C. Thompson, B. J. Kim, M. F. Toney, J. M. J. Fréchet, *J. Am. Chem. Soc.* **2008**, *130*, 16324.
- [22] Scattering from P3HT crystallites with the (100) layer normal oriented perfectly perpendicular to the substrate are not observed in the grazing incidence geometry. As a result, using the grazing incidence geometry does not allow for the complete measurement of the orientation of P3HT layers as a function of the polar angle  $\chi$ . Instead, we will refer to the azimuthal distribution of P3HT layer orientations observed as a function of  $\beta$ , where  $\beta = 90^\circ$  is vertical in the GIXS images.
- [23] J. L. Baker, L. H. Jimison, S. Mannsfeld, S. Volkman, S. Yin, V. Subramanian, A. Salleo, A. P. Alivisatos, M. F. Toney, *Langmuir* **2010**, *26*, 9146.
- [24] D. W. Breiby, O. Bunk, J. W. Andreasen, H. T. Lemke, M. M. Nielsen, *J. Appl. Crystallogr.* **2008**, *41*, 262.
- [25] S. C. B. Mannsfeld, A. Virkar, C. Reese, M. F. Toney, Z. N. Bao, *Adv. Mater.* **2009**, *21*, 2294.
- [26] R. J. Kline, M. D. McGehee, M. F. Toney, *Nat. Mater.* **2006**, *5*, 222.
- [27] S. Cho, K. Lee, J. Yuen, G. M. Wang, D. Moses, A. J. Heeger, M. Surin, R. Lazzaroni, *J. Appl. Phys.* **2006**, *100*, 114503.
- [28] H. C. Yang, T. J. Shin, Z. N. Bao, C. Y. Ryu, *J. Polym. Sci., Part B: Polym. Phys.* **2007**, *45*, 1303.
- [29] R. Zhang, B. Li, M. C. Iovu, M. Jeffries-EL, G. Sauvé, J. Cooper, S. J. Jia, S. Tristram-Nagle, D. M. Smilgies, D. N. Lambeth, R. D. McCullough, T. Kowalewski, *J. Am. Chem. Soc.* **2006**, *128*, 3480.
- [30] H. C. Yang, T. J. Shin, L. Yang, K. Cho, C. Y. Ryu, Z. N. Bao, *Adv. Funct. Mater.* **2005**, *15*, 671.
- [31] J. F. Chang, B. Q. Sun, D. W. Breiby, M. M. Nielsen, T. I. Solling, M. Giles, I. McCulloch, H. Sirringhaus, *Chem. Mater.* **2004**, *16*, 4772.
- [32] X. N. Yang, J. K. J. van Duren, M. T. Rispens, J. C. Hummelen, R. A. J. Janssen, M. A. J. Michels, J. Loos, *Adv. Mater.* **2004**, *16*, 802.
- [33] R. J. Kline, M. D. McGehee, E. N. Kadnikova, J. S. Liu, J. M. J. Fréchet, *Adv. Mater.* **2003**, *15*, 1519.
- [34] R. J. Kline, M. D. McGehee, E. N. Kadnikova, J. S. Liu, J. M. J. Fréchet, M. F. Toney, *Macromolecules* **2005**, *38*, 3312.
- [35] K. A. Singh, G. Sauve, R. Zhang, T. Kowalewski, R. D. McCullough, L. M. Porter, *Appl. Phys. Lett.* **2008**, *92*.
- [36] B. Wunderlich, *J. Chem. Phys.* **1958**, *29*, 1395.
- [37] M. Avrami, *J. Chem. Phys.* **1939**, *7*, 1103.
- [38] W. A. Johnson, R. F. Mehl, *Trans. Am. Inst. Min. Metall. Eng.* **1939**, *135*, 416.
- [39] J. M. Schultz, *Polymer Materials Science*, Prentice Hall, New Jersey **1974**.
- [40] R. M. R. Wellen, M. S. Rabello, *J. Mater. Sci.* **2005**, *40*, 6099.
- [41] R. J. Young, P. A. Lovell, *Introduction to polymers*, Chapman & Hall, London, New York **1991**.
- [42] M. Campoy-Quiles, T. Ferenczi, T. Agostinelli, P. G. Etchegoin, Y. Kim, T. D. Anthopoulos, P. N. Stavrinou, D. D. C. Bradley, J. Nelson, *Nat. Mater.* **2008**, *7*, 158.
- [43] J. W. Kiel, B. J. Kirby, C. F. Majkrzak, B. B. Maranville, M. E. Mackay, *Soft Matter* **2010**, *6*, 641.
- [44] M. T. Rispens, A. Meetsma, R. Rittberger, C. J. Brabec, N. S. Sariciftci, J. C. Hummelen, *Chem. Commun.* **2003**, 2116.
- [45] A. Swinnen, I. Haeldermans, P. Vanlaeke, J. D'Haen, J. Poortmans, M. D'Olieslaeger, J. V. Manca, *Eur. Phys. J.: Appl. Phys.* **2006**, *36*, 251.